Axial Plus Tangential Entry Swirling Jet

I. K. Toh, D. Honnery and J. Soria

Laboratory for Turbulence Research in Aerospace and Combustion,
Department of Mechanical and Aerospace Engineering, Monash University,
3800 Melbourne, Vic. Australia
francis.toh@eng.monash.edu.au

ABSTRACT

An experimental investigation of swirling jets with initial velocity distributions different from previous studies is presented. Jets with initial azimuthal velocity profiles that peak near the jet edge while having very little swirl at the jet core are produced using an axial plus tangential entry swirl generator. Jets with Reynolds numbers of ≈ 1700 and swirl intensity ranging from a non-swirling reference case to a very high swirl case with vortex breakdown are studied. The axial, radial and azimuthal velocity components, with their respective fluctuation components are measured using particle image velocimetry (PIV). It is observed that increasing swirl promotes the centerline axial velocity decay and jet spread. PIV velocity field measurements on swirling jets on the verge of or immediately after vortex breakdown shows that vortex breakdown can be seen in the instantaneous velocity fields, but is lost in the time-averaged velocity field.

1. INTRODUCTION

The large scale effects of swirl in fluid flows have been appreciated for many decades. In general, the imposition of swirl in a free turbulent jet increases jet spread, jet width, jet growth, jet decay, entrainment, and turbulence intensity [2] [5]. When the degree of swirl is sufficiently high, vortex breakdown occurs. There are various forms of vortex breakdown reported in the literature. However, they all share a common feature: an abrupt deceleration of the flow near the jet axis leading to the formation of a stagnation point, as if a solid obstacle had been introduced into the flow [1].

There are a number of ways of generating a swirling jet, namely axial plus tangential entry [2], direct rotation of a perforated plate, pipe or honeycomb [1, 5] and adjustable vanes. Different swirl generation mechanisms produce swirling jets with different initial azimuthal velocity distributions, ranging from solid body rotation to a near-free vortex. The initial velocity distributions can have a profound effect on the resultant flow. [3] achieved vortex breakdown at a swirl number of 0.48 using a swirling jet with a free vortex type azimuthal velocity distribution. This critical swirl number is significantly lower than 0.6 reported in[2]. For the present study, an axial plus tangential entry swirl nozzle is used to generate swirling jets with a high azimuthal velocity component near the jet edge, and very little swirl near the jet core.

The aim of the present experimental study is to investigate the characteristics of a swirling jet with initial azimuthal velocity profiles that differ from previous studies. Particular attention is paid to the jets that are on the verge of and immediately after vortex breakdown.

2. METHODOLOGY

The swirl generator used in this study is shown in figure 1. Air supply to the main jet is separate from the air supply to the tangential injectors. This allows the flow rate of the main axial jet and the tangential injectors to be varied independently. To enable PIV measurements, the main axial jet supply was seeded with olive oil droplets of approximately $1\mu m$ in diameter. A settling chamber consisting of multiple screens and a honeycomb structure was used to reduce the turbulence intensity and remove the radial and azimuthal velocity component present in the flow. The main axial supply was then contracted by an area ratio of 16 to 1 at the end of the settling chamber. The unseeded tangential air supply was directed into an annulus reservoir, then injected tangentially into the main axial supply through eight $1mm$ diameter cross section injectors. The combined flow was discharged through a $12mm$ diameter orifice. The coordinate system used in this study is shown in figure 1. It consists of axial (x), radial (r) and azimuthal (θ) components with velocity u, v and w respectively. The time averaged velocities are denoted as U, V and W with their fluctuation components u', v' and w'.
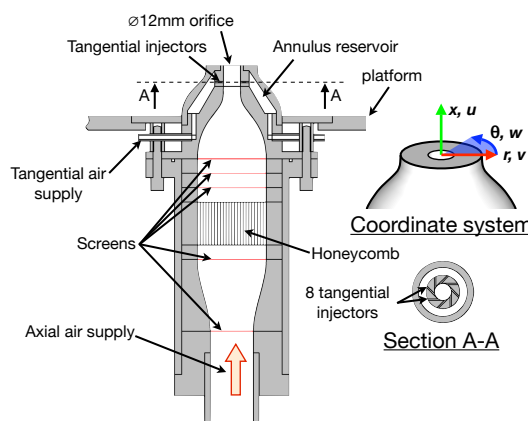

Figure 1: Swirl nozzle design and coordinate system.

The experimental apparatus is shown in figure 2. The swirl nozzle was mounted on a $370mm \times 370mm$ square metal plate. The $600mm \times 600mm$ square cross sectional test section was isolated from the surrounding air movement using covers extending from $x/D_0 = 30$ below the orifice to $x/D_0 = 70$ above the orifice. A Qanta System Dual Nd:YAG laser system with an output wavelength of $532nm$ was used to illuminate the seeding particles. The laser is capable of producing two $200mJ$ pulses of $5 - 6ns$ duration at a repetition rate of up to $10Hz$. System timing was controlled by a timing computer operated on a Real Time Application Interface (RTAI) operating system. The timing signals are monitored by an oscilloscope. The images
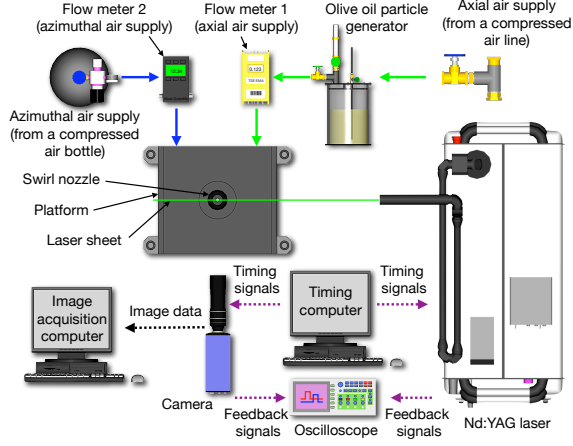
Figure 2: Experimental apparatus.

Table 1: MCCDPIV processing parameter

Parameter	$x-r$ plane	$r-\theta$ plane
Image location	0 - 3.89D_0	0.08D_0
Image area	$5.84D_0 \times 3.89D_0$	$1.83D_0 \times 1.83D_0$
CCD array	$4008px \times 2672px$	$1800px \times 1800px$
spatial resolution	$57.2px/mm$	$82.1px/mm$
Sample size	1000	1000
First IW size	$32px \times 32px$	$64px \times 64px$
Second IW size	$16px \times 16px$	$32px \times 32px$
Vector spacing	$8px$	$16px$

required for PIV were acquired using a PCO4000 digital camera operated in a double shutter mode. Images obtained were stored in an image acquisition computer. Images in both the $x-r$ plane and $r-\theta$ plane were acquired. The laser sheet was rotated $90°$ into the $r-\theta$ plane and a high reflective mirror was place at $x/D_0 \approx 35$ to reflect the object into the camera when images in the $r-\theta$ plane were acquired. Orientation of the camera was such that a CCD array of $4008px \times 2672px$ was used for images in the $x-r$ plane, and a sub-domain of the CCD array of size $1800px \times 1800px$ was used for images in the $r-\theta$ plane. A $200mm$ Nikkor lens was used to project the object onto the CCD array. The PIV imaging parameters are tabulated in table 1. Note that the images are contaminated by laser light reflection when the image plane is too close to the orifice. Therefore, the images in the $r-\theta$ plane were taken slightly downstream at $x/D_0 = 0.08$. The conditions measured at $x/D_0 = 0.08$ are used as initial conditions in this study.

The single exposed image pairs were analysed using the multi-grid cross correlation digital particle image velocimetry (MCCDPIV) described in Soria et. al. (1999) [7] and Soria (1996) [6]. The algorithm uses an iterative and adaptive technique to increase the dynamic range of the velocity, and reduce the random and bias error. This is done by offsetting the discrete sampling window in the second exposure adaptively by an amount approximately equal to the distance traveled by the particle during the time separation between the two images. The algorithm also incorporates a local cross-correlation function multiplication method [4] to improve the search for the location of the maximum value of the cross-correlation function. For the sub-pixel peak calculation, a two dimensional Gaussian function model was used to find the location of the maximum of the cross-correlation function using the least mean square value. A median test [9] and a dynamic mean value operator test [9]

were applied subsequently to validate the MCCDPIV data field. Following data validation, the in-plane velocity components in the coordinate directions were computed by dividing the measured displacement in each interrogation window by the time between the exposures of the image pair (δt) and the optical magnification. The out-of-plane vorticity (ω_z) was calculated using the χ^2 fitting of the measured velocity field [6]. The PIV processing parameters are tabulated in table 1.

3. RESULTS

A swirling jet can be characterized using two non-dimensional parameters, the Reynolds number (Re) and the swirl number (S). The Reynolds number is based on the average axial velocity at the orifice ($\bar{U}_0$) and the swirl nozzle exit diameter (D_0),

$$Re = \frac{\bar{U}_0 D_0}{\nu}. \tag{1}$$

The swirl number is defined as the ratio of axial flux of azimuthal momentum to the axial flux of axial momentum multiplied by the equivalent swirl nozzle exit radius [2],

$$S = \frac{2\pi\rho \int_0^R r^2 UW \, dr}{2\pi\rho \left[\int_0^R r \left(U^2 - \frac{1}{2}W^2 + \bar{u'^2} - \frac{1}{2}(\bar{w'^2} - \bar{v'^2}) \right) dr \right] \times R}. \tag{2}$$

Six experimental conditions with $Re \approx 1700$ and a swirl number range of $S_1 = 0$ to 3.42 are investigated in the present study. The Reynolds number and swirl number, as well as the maximum axial and azimuthal velocity at the swirl nozzle exit (U_{m0} and W_{m0}) are tabulated in table 2. The swirl number calculated are much higher than those in the previous studies because of the initial velocity profile, as discussed in [8]. As such, for the present study, this swirl number is only used as a measure of the degree of swirl, but not as a scaling parameter nor a criteria to predict the occurrence of vortex breakdown.

Table 2: Experimental conditions

Re	U_{m0} (m/s)	W_{m0} (m/s)	W_{m0}/U_{m0}	S
1667	2.366	0.000	0.000	0.00
1770	2.540	0.742	0.292	0.11
1765	2.787	2.094	0.751	0.56
1744	2.675	3.307	1.236	1.70
1675	2.898	3.903	1.347	2.63
1690	3.285	4.262	1.297	3.42

The radial distribution of initial velocity profiles are presented in figure 3. The velocities are normalized by the time-averaged local maximum axial velocity, U_m, at $x/D_0 = 0$. The radial location r is normalized by the swirl nozzle exit diameter (D_0). For figure 3a and 3b, every 5th data point is presented, but the line is drawn using all available data points. For the non-swirling case, the initial axial velocity profile approaches a top-hat profile. As swirl is introduced and increased, the azimuthal velocity component interacts with the axial velocity component. This interaction is commonly observed in swirling jets studies [1] and [3]. A local maximum is produced near the centreline axis ($r/r_{1/2} \approx 0$), while axial velocity decreases at the jet edge. For higher swirl cases ($S_1 = 1.70$), a secondary axial velocity peak is formed at $r/D_0 \approx 0.5$. The axial velocity at the vicinity of the jet axis close to the nozzle exit for higher swirl cases is suppressed by the adverse axial pressure gradient induced by the azimuthal velocity component. This results in the secondary axial velocity peak exceeding the centreline axial velocity for $S = 2.63$ and 3.42.
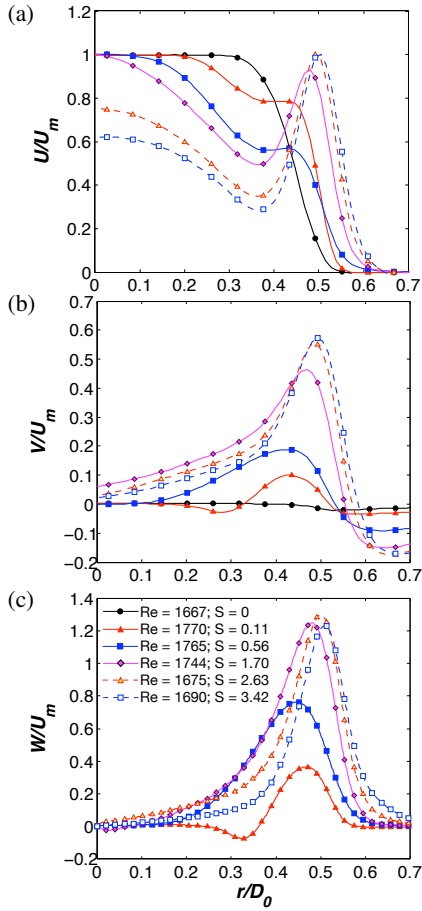
Figure 3: Radial distribution of normalized initial (a) axial, (b) radial and (c) azimuthal velocity at $x/D_0 = 0$.

Figure 4: Instantaneous velocity field for $S = 2.63$. Every second vector presented.

The distribution of the radial velocity component shown in figure 3b is significant compared to the axial velocity component. For the higher swirl cases ($S = 2.63$ and 3.42) the maximum radial velocity component is approximately $0.6U_m$.

Figure 3c shows the radial distribution of the normalized azimuthal velocity. The azimuthal velocity distributions differ from previous studies, it is neither solid body rotation such as that in [1] and [5] nor a free vortex type distribution found in [3]. There is very little azimuthal velocity component for $r/D_0 < 0.2$. The azimuthal velocity starts to increase dramatically from $r/D_0 = 0.2$, and reaches the maximum at $r/D_0 \approx 0.5$ before dropping to zero outside of the jet ($r/r_{1/2} > 1$). The magnitude of the azimuthal velocity increases as swirl number increases. The ratio of the maximum azimuthal to axial velocity (W_m/U_m) is approximately 1.2 - 1.3 for $S = 1.70$, 2.63 and 3.42. Note that W_m/U_m for these three swirl cases are nearly similar because U_m is larger for the higher swirl case.

The velocity field in the $r - x$ plane for $S = 2.63$ is specifically chosen and presented in figure 4. This swirl condition represent swirling jet on the verge of, or right after vortex breakdown. Regions of low axial velocity starts to appear and disappear in the instantaneous velocity field in the $S = 1.70$ case (not shown). As swirl number increases, the region of low axial velocity enlarges, and the frequency of its appearance increases. Vortex breakdown features such as stagnation points, region of low axial velocity and reverse flow occur from time to time, as observed in $S = 2.63$ (figure 4). However, at this swirl number, these features are both spatially and temporally unsteady. This
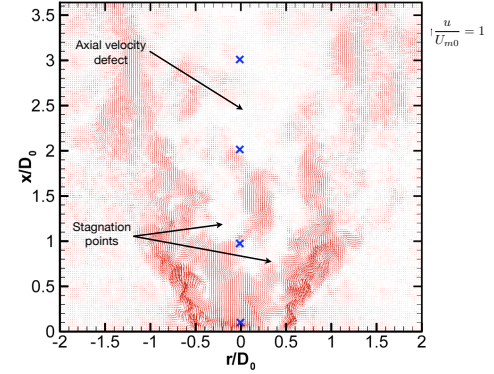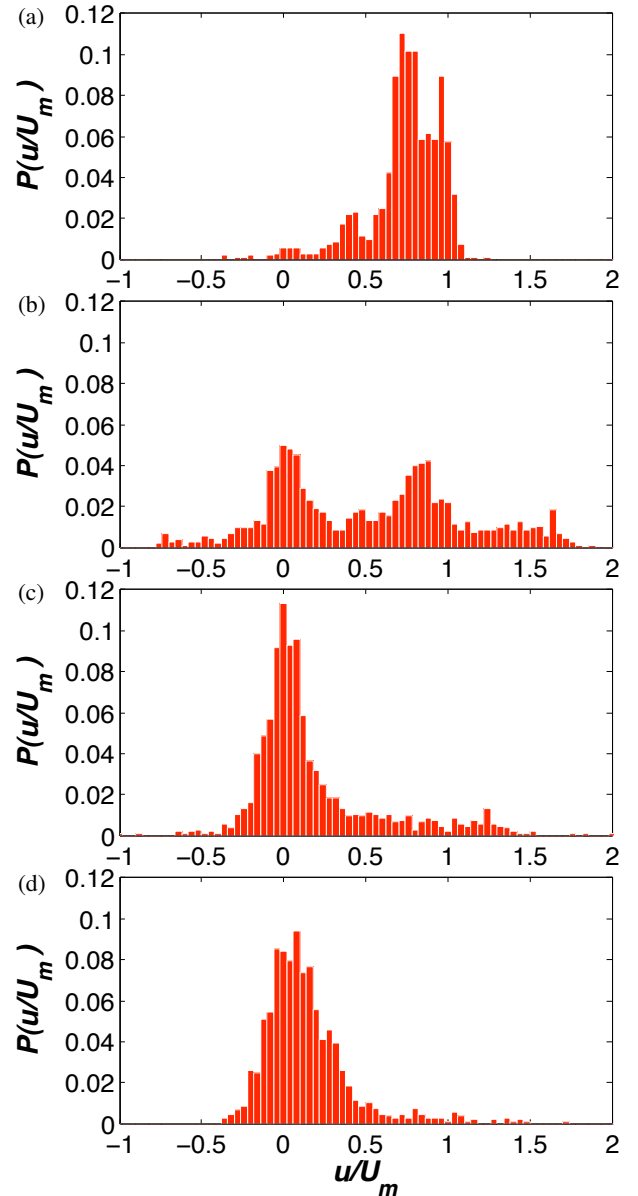

Figure 5: Probability density function of u/U_m at (a) $x/D_0 = 0.16$; (b) 1.00; (c) 2.03 and (d) 2.96. Sample size = 1000.

observation is consistent with [5] in the swirl number region close to or immediately after vortex breakdown.

In order to better illustrate this phenomena, the probability density function of the instantaneous axial velocity at various locations along the centerline axis marked in figure 4 ($x/D_0 = 0.16$, 1.00, 2.03 and 2.96) are constructed (figure 5). $P(u/U_m)$ is the number of occurrence normalized by the sample size. The instantaneous axial velocities u are normalized by the time-averaged local maximum axial velocities U_m at the corresponding axial locations. Close to the swirl nozzle exit ($x/D_0 = 0.16$), the axial velocity component is predominantly in the $0.4 - 1.1U_m$ range, with occasional fluctuation outside of this range. At $x/D_0 = 1$, the axial location where stagnation points start to appear and disappear, the probability density function of the axial velocity shows two distinct peaks of similar magnitude. This indicates that the flow at that location frequently switches between two distinct states, with one being close to stagnant or even slightly reverse. The probability density functions of the axial velocity component at similar axial location, but different radial locations ($r/D_0 < 0.3$, not shown) also show this double peak behavior. This observation suggests that these stagnation points and reverse flow either appear and disappear, or they are oscillating the region. Further downstream of the swirl nozzle exit ($x/d_0 = 2.03$ and 2.96), the probability density function shows only one single peak, but with significant portion of the axial velocity component being in the negative region (reverse flow).

These vortex breakdown features at that swirl number do not appear in the time-averaged measurements. For example, the time-averaged centerline axial velocity decay along the centerline axis (U_c/U_{c0}, U_{c0} = centerline axial velocity at the swirl nozzle exit) presented in figure 6a does not show any stagnation points nor reverse flow for $S = 2.63$, even though they have been observed in the instantaneous velocity field. Clear signs of vortex breakdown are only observed when swirl number is significantly higher ($S = 3.41$), in which a stagnation point followed by a reverse flow is observed at $x/D_0 = 0.5$ to 3.

Nevertheless, the flow ($S = 2.63$) exhibit many similar characteristics as $S = 3.41$. Figure 6b shows the normalized half-width ($r_{1/2}$) plotted against the normalized axial location. The half-width $r_{1/2}$ is the radial location where $U(x, r_{1/2}) = 0.5U_m(x)$. The half-width is often used as a measure of the width of the jet, and hence an indication the jet spread. It appears that the jet spread of $S = 2.63$ and 3.41 are very similar up to $x/D_0 \approx 8$. This is because at such high swirl number, and in the near field region, vortex breakdown plays a dominant role in the jet spread process. One difference between the two is that the initial jet spread ($x/D_0 < 2$) for $S = 3.41$ is slightly higher than $S = 2.63$. This is because when swirl number increases post-vortex breakdown, the axial location of the vortex breakdown shifts upstream, hence causes the jet to spread out earlier. The jet spread behavior also agree with the observation reported in [5], in which the effect of swirl on jet spread is less significant at low swirl number, but increases dramatically when the jet approaches vortex breakdown.

4. CONCLUSION

For swirling jets on the verge or immediately after vortex breakdown, many vortex breakdown features observed are to be transient, and are lost lost during the averaging processes and hence go undetected in the time-averaged measurements. This questions the ability of older studies to accurately detect the early stages of vortex breakdown without the aid of instantaneous field measurement techniques such as PIV.
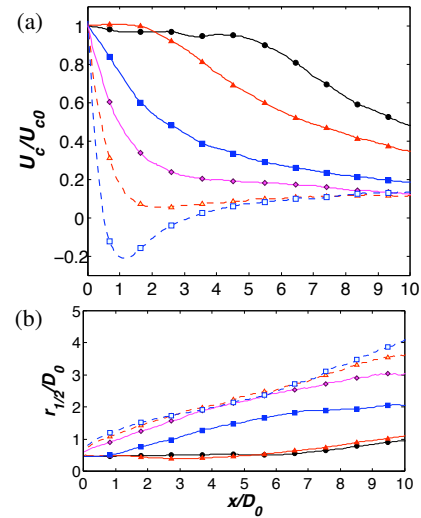

Figure 6: Normalized (a) centerline axial velocity decay; (b) half-width versus the normalized axial coordinate. Every 20th data point shown.

REFERENCES

[1] Billant, P., Chomaz, J., Huerre, P.: Experimental study of vortex breakdown in swirling jets. J. Fluid Mech. **376**, 183–219 (1998)

[2] Chigier, N.A., Chervinsky, A.: Experimental investigation of swirling vortex motion in jets. J. Appl. Mech. pp. 443–451 (1967)

[3] Farokhi, S., Taghavi, R., Rice, E.J.: Effect of initial swirl distribution on the evolution of a turbulent jet. AIAA Journal **27**(6), 700–706 (1989)

[4] Hart, D.: Piv error correction. Exp. Fluids **29**, 13–22 (2000)

[5] Liang, H., Maxworthy, T.: An experiment investigation of swirling jets. J. Fluid Mech. **525**, 115–159 (2005)

[6] Soria, J.: An investigation of the near wake of a circular cylinder using a video-based digital cross-correlation particle image velocimetry technique. Exp. Thermal and Fluid Sc. **12**, 221–233 (1996)

[7] Soria, J., Carter, J., Kostas, J.: High resolution multi-grid cross correlation digital piv measurement of a turbulent starting jet using half-frame-image-shift film recording. Optics and Laser Tech. **31**, 3–12 (1999)

[8] Toh, I.K., Damon, D., Soria, J.: Axial plus tangential entry swirling jet. In: Fifth Australian Conference on Laser Diagnostics in Fluid Mechanics and Combustion, pp. 127–130. University of Western Australia, Perth, Australia (2008)

[9] Westerweel, J.: Efficient detection of spurious vectors in particle image velocimetry data. Exp. Fluids **16**, 236–247 (1994)